Measurement Science and Technology

PAPER

GNSS/INS/ODO/wheel angle integrated navigation algorithm for an all-wheel steering robot

To cite this article: Zaixing Zhang *et al* 2021 *Meas. Sci. Technol.* **32** 115122

IOP Publishing Measurement Science and Technology

Meas. Sci. Technol. **32** (2021) 115122 (9pp) https://doi.org/10.1088/1361-6501/ac17fb

GNSS/INS/ODO/wheel angle integrated navigation algorithm for an all-wheel steering robot

Zaixing Zhang, Xiaoji Niu, Hailiang Tang, Qijin Chen and Tisheng Zhang*

GNSS Research Center, Wuhan University, Wuhan, Hubei 430079, People's Republic of China

E-mail: zts@whu.edu.cn

Received 8 May 2021, revised 14 July 2021
Accepted for publication 27 July 2021
Published 13 August 2021

Abstract

To suppress the positioning error of wheeled robots in global navigation satellite system (GNSS) denial environments, kinematic constraints should be fully utilized. However, many wheeled robots have independent steering mechanisms for each wheel to move more flexibly, which do not meet the nonholonomic constraint in the vehicle frame. Hence, the conventional GNSS/inertial navigation system (INS)/ODO (odometer) integrated navigation algorithm (GIOW algorithm) is no longer suitable. We propose a GIOW algorithm to meet the need for all-wheel steering robot positioning. In the proposed algorithm, odometer speed and wheel angle are employed together to construct a kinematic constraint for wheeled robots, which can constrain the rapid drifting error of INS. Moreover, the odometer scale factor and wheel angle error are augmented into the error state of the extended Kalman filter to be estimated and compensated online. Field tests were carried out in an open-sky environment with a wheeled robot, which can run in both corner steering mode and all-wheel steering mode. The experimental results showed that the proposed algorithm can be applied to not only the corner steering motion model but also the all-wheel steering motion model. The accuracy of the proposed algorithm was almost the same as that of the conventional GNSS/INS/ODO algorithm in the corner steering motion model. In the all-wheel steering motion model, the accuracy of the proposed algorithm was maintained.

Keywords: GNSS/INS integration, all-wheel steering, nonholonomic constraint, odometer, wheel angle

(Some figures may appear in colour only in the online journal)

1. Introduction

With the rapid development of the robot industry, accurate and continuous positioning for robots has become particularly important. The integration system of the global navigation satellite system (GNSS) and low-cost inertial navigation system (INS) has been extensively applied in the navigation field, which can fully utilize the advantages of the two subsystems to provide continuous position, velocity, and attitude [1–3]. However, GNSS signal interference and outages frequently arise in urban environments, and the error of low-cost INS accumulates quickly without GNSS assistance, which leads to rapid deterioration of the positioning accuracy of the integration system [4, 5]. Hence, it is urgent for robots to maintain positioning accuracy when GNSS signals are blocked.

An odometer, with low cost and good reliability, is a commonly used sensor for wheeled carriers. GNSS, INS, and odometer (ODO) fusion navigation is currently a mainstream solution. However, most GNSS/INS/ODO

[*] Author to whom any correspondence should be addressed.

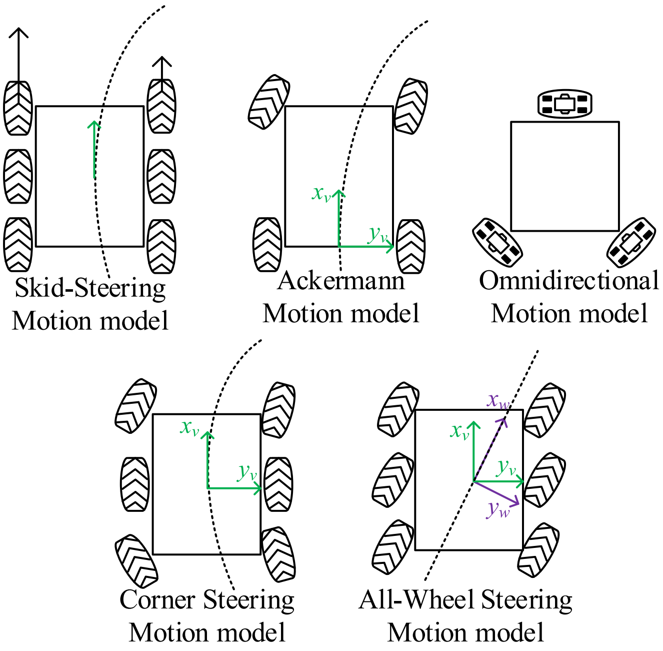

Figure 1. Robot motion models.

integration solutions are based on vehicular constraints and do not consider robot kinematic constraints, which are called conventional vehicular constraint algorithms in this paper. The conventional vehicular constraint algorithm is based on a nonholonomic constraint (NHC) in a vehicle frame [6–9]. The vehicle frame (v-frame) is the vehicle's body frame and represents the orientation of the vehicle. The NHC in the v-frame refers to the fact that if wheels do not skid or jump, the v-frame velocity in the plane perpendicular to the longitudinal direction is almost zero. The theory is valid in the vehicle motion model (Ackermann motion model), but not in other robot motion models.

Howard *et al* summarized five motion models of wheeled robots [10], as shown in figure 1. The skid-steering motion model has no steering mechanism, and the steering is carried out by the differential speed of wheels on both sides. Wheel slips need to be considered in the kinematic constraint for this model. Jingang *et al* developed a kinematic modeling method to analyze the skid-steering motion model [11]. The omnidirectional motion model is the most capable model, allowing motion in any direction in the local tangent plane. The speed of each wheel is represented by the translation and rotation vectors in the robot frame [12]. These two models are not the focus of this paper.

The Ackermann steering and corner steering motion models are less flexible models because their linear velocities are constrained along the longitudinal direction of the v-frame. The Ackermann motion model is extensively employed in four-wheeled carriers, while the corner steering motion model is usually used in six-wheeled robots. The conventional vehicular constraint algorithm is applicable to these two models and has been exhaustively studied for decades. Here, an odometer is installed on the nonsteer wheel to provide longitudinal velocity observation in the v-frame. The nonsteer wheel refers to the rear wheel in the Ackermann motion model or the middle wheel in the corner steering motion model. The NHC can be combined with the odometer, and therefore a three-dimensional velocity observation at the nonsteer wheel in the v-frame is constructed to constrain the drifting error of the INS [8].

The all-wheel steering motion model also allows motion in any direction in the local tangent plane but is restricted by the NHC in wheel frame. The wheel frame (w-frame) represents the orientation of the middle wheel, which has a horizontal angle with the v-frame, as shown in figure 1. The angle is called wheel angle in this paper. Since the movement direction of this model is along the longitudinal direction of the w-frame, the odometer cannot be employed independently in this model. Therefore, the wheel angle needs to be considered in the navigation algorithm.

In fact, angle information has been used in some conventional vehicular constraint methods. Gao utilized the steering angle to constrain the tangent of the lateral and longitudinal velocities at the front wheels of a vehicle, which were derived from odometer and yaw rate sensors. The biases and scale factors of the steering angle were estimated in the extended Kalman filter (EKF) [13, 14]. Dixon *et al* obtained the odometer speed of four wheels and steering angle from the antilock brake system of a vehicle and built redundant expressions describing the Ackerman motion model, 'which allowed for better distance measurements via redundancy and additionally provided relative yaw angle measurements by differencing wheel speed' [15]. The steering angle is regarded as redundant information in the above methods, which makes the algorithm robust. However, the steering angle refers to the turning angle of the vehicle, while the wheel angle is the angle of the wheel relative to the vehicle. In figure 1, the steering angle of the all-wheel steering motion model is zero, but the wheel angle is not.

Considering the wheel angle, we propose a GNSS/INS/ODO/wheel angle integrated navigation algorithm (GIOW algorithm) for the all-wheel steering motion model. This algorithm can also be applicable to the corner steering motion model. The key points of our work are as follows:

- Error state vector construction: model the errors of odometer and steering mechanism, augment odometer scale factor and wheel angle error into the error state of the EKF, and then estimate and compensate for them online.
- Robot kinematic constraint: employ the NHC combined with the odometer speed and wheel angle to construct a w-frame velocity observation.

The remainder of this paper is organized as follows. Section 2 describes the details of the GIOW algorithm. In section 3, the analysis and discussion of the experimental results are presented to evaluate the performance of the algorithm. Section 4 discusses conclusions and future work.

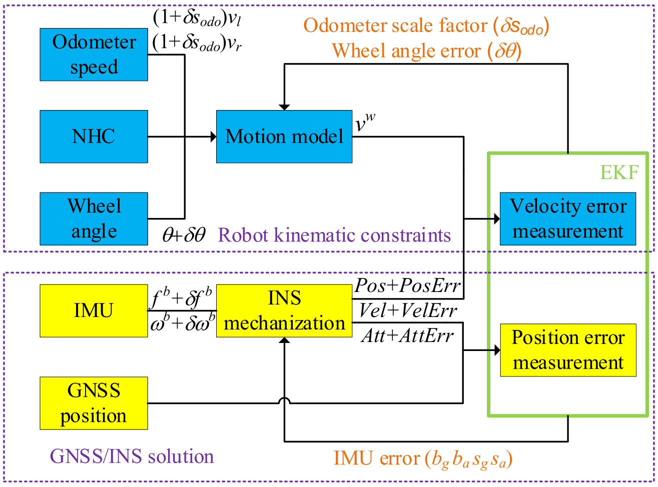

Figure 2. Algorithm overview.

2. Methodology

The GIOW algorithm adds robot kinematic constraints based on the GNSS/INS solution, as shown in figure 2. The GNSS/INS solution is a classic method where the position error measurement is input into the EKF to constrain the drifting error of the INS [16, 17]. The procedure of the robot kinematic constraint is as follows:

(a) Obtain the w-frame longitudinal velocity by the odometer speed and the wheel angle. Construct a three-dimensional velocity observation by combining the NHC with the longitudinal velocity.
(b) Calculate the difference between the w-frame velocity observation and the velocity result derived by INS.
(c) Estimate the error state of the EKF, including the navigation error (position error, velocity error, and attitude error), inertial measurement unit (IMU) error, odometer scale factor, and wheel angle error.
(d) The navigation error is used to correct the position result, velocity result, and attitude result. The IMU error, odometer scale factor, and wheel angle error are compensated.

The error state equation and observation equations are the core of the EKF. In section 2.1, the error state and error state equation are constructed. Then the observation equation is derived in section 2.2.

2.1. Error state vector

As a part of the error state, the navigation error includes the position error $\delta\boldsymbol{r}^n$, velocity error $\delta\boldsymbol{v}^n$, and attitude error ϕ. The perturbation models of these errors are described in [18].

The IMU is composed of a three-axis gyroscope and a three-axis accelerometer. The error model of the gyroscope can be expressed as

$$\begin{aligned}\hat{\boldsymbol{\omega}}_{ib}^{b} &= (\mathbf{I}+\boldsymbol{s}_g)\boldsymbol{\omega}_{ib}^{b}+\boldsymbol{b}_g+\boldsymbol{w}_g\\ \delta\boldsymbol{\omega}_{ib}^{b} &= \hat{\boldsymbol{\omega}}_{ib}^{b}-\boldsymbol{\omega}_{ib}^{b}=\boldsymbol{s}_g\boldsymbol{\omega}_{ib}^{b}+\boldsymbol{b}_g+\boldsymbol{w}_g\end{aligned} \tag{1}$$

where $\delta\boldsymbol{\omega}_{ib}^{b}$ is the error of the angular velocity, $\boldsymbol{b}_g$ is the residual biases, $\boldsymbol{s}_g$ is the residual scale factors, and $\boldsymbol{w}_g$ is the measurement noise. The error model of accelerometer can be described as

$$\begin{aligned}\hat{\boldsymbol{f}}^{b} &= (I+\boldsymbol{s}_a)\boldsymbol{f}^{b}+\boldsymbol{b}_a+\boldsymbol{w}_a\\ \delta\boldsymbol{f}^{b} &= \hat{\boldsymbol{f}}^{b}-\boldsymbol{f}^{b}=\boldsymbol{s}_a\cdot\boldsymbol{f}^{b}+\boldsymbol{b}_a+\boldsymbol{w}_a\end{aligned} \tag{2}$$

where $\delta\boldsymbol{f}^{b}$ is the error of the specific force, $\boldsymbol{b}_a$ is the residual biases, $\boldsymbol{s}_a$ is the residual scale factors, and $\boldsymbol{w}_a$ is the measurement noise.

The measurement noise of the gyroscope and accelerometer, $\boldsymbol{w}_g$ and $\boldsymbol{w}_a$, are integrated into angle random walk (ARW) and velocity random walk (VRW), respectively. Values of the VRW and ARW are usually determined through the Allan variance analysis [19]. The biases and scale factors of the gyroscope and accelerometer are commonly modeled as first-order Gauss-Markov processes [20], where $\boldsymbol{w}_{bg}$, $\boldsymbol{w}_{ba}$, $\boldsymbol{w}_{sg}$, and $\boldsymbol{w}_{sa}$ are the noise of the evolution of these errors.

There are errors of the given speed from the odometer and the given wheel angle from the steering mechanism. The odometer speed is correlated with the pulse number per second sensed by the odometer, the tooth number per rotation, and the diameter of the wheel tire [14]. The wheel diameter is affected by tire pressure, temperature, and tire wear; therefore, the odometer scale factor should be considered [21]. The error model of the odometer speed can be expressed by

$$\hat{v}_{\mathrm{odo}}=(1+s_{\mathrm{odo}})\frac{N_{\mathrm{Pulse}}\pi d}{N_{\mathrm{Teeth}}} \tag{3}$$

where s_{odo} is the odometer scale factor, N_{Pulse} is the number of pulses per second, N_{Teeth} is the number of teeth per rotation, and d is the wheel diameter.

The steering mechanism will be worn after long term use, and the wheel angle error cannot be ignored. The error model of the wheel angle can be expressed by

$$\hat{\theta}=\theta+\delta\theta \tag{4}$$

where $\delta\theta$ is wheel angle error.

Since the odometer scale factor and the wheel angle error change slowly, they are modeled as random walks with small driving noise,

$$\begin{aligned}\dot{s}_{\mathrm{odo}} &= w_{\mathrm{odo}}\\ \delta\dot{\theta} &= w_{\theta}\end{aligned} \tag{5}$$

where w_{odo} and w_{θ} are driving noise.

In conclusion, the error state vector is constructed as

$$\boldsymbol{x}=\left[(\delta\boldsymbol{r}^{n})^{\mathrm{T}}\ \ (\delta\boldsymbol{v}^{n})^{\mathrm{T}}\ \ \boldsymbol{\phi}^{\mathrm{T}}\ \ \boldsymbol{b}_g{}^{\mathrm{T}}\ \ \boldsymbol{b}_a{}^{\mathrm{T}}\ \ \boldsymbol{s}_g{}^{\mathrm{T}}\ \ \boldsymbol{s}_a{}^{\mathrm{T}}\ \ s_{\mathrm{odo}}\ \ \delta\theta\right]^{\mathrm{T}}. \tag{6}$$

And the error state equation can be expressed as

$$\begin{aligned}\dot{\boldsymbol{x}}(t) &= \mathbf{F}(t)\boldsymbol{x}(t)+\mathbf{G}(t)\boldsymbol{w}(t)\\ \boldsymbol{w}(t) &= \left[\boldsymbol{w}_g{}^{\mathrm{T}}\ \ \boldsymbol{w}_a{}^{\mathrm{T}}\ \ \boldsymbol{w}_{bg}{}^{\mathrm{T}}\ \ \boldsymbol{w}_{ba}{}^{\mathrm{T}}\ \ \boldsymbol{w}_{sg}{}^{\mathrm{T}}\ \ \boldsymbol{w}_{sa}{}^{\mathrm{T}}\ \ w_{\mathrm{odo}}\ \ w_{\theta}\right]^{\mathrm{T}}\end{aligned} \tag{7}$$

where $\mathbf{F}$ is the dynamics matrix [18], $\mathbf{G}$ is the noise-input mapping matrix and $\boldsymbol{w}$ is the noise vector.

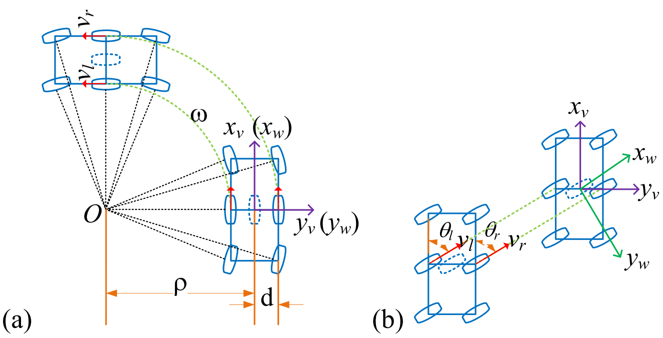

Figure 3. Robot motion model. (a) Corner steering motion model. (b) All-wheel steering motion model.

2.2. Robot kinematic constraint

The GNSS observation equation in the GNSS/INS solution has been given in previous work [18]. The observation equation of the robot kinematic constraint is elaborated in this section.

The details of the corner steering motion model and the all-wheel steering motion model are shown in figure 3(a) and figure 3(b), respectively. If both the left middle wheel and the right middle wheel are equipped with odometers, the virtual center wheel (the center of two wheels) is considered in the GIOW algorithm. Otherwise, the wheel equipped with odometer is considered. The following takes the virtual center wheel as an example.

The origin of the v-frame is the virtual center wheel. Its X-axis points toward the forward direction of the vehicle's motion, its Y-axis points toward the right side of the vehicle, and its Z-axis completes a right-handed orthogonal frame, i.e. forward-transversal-down. The w-frame has its origin coinciding with that of the v-frame. Its X-axis points toward the forward direction of the middle wheels, its Z-axis coincides with that of the v-frame, and its Y-axis completes a right-handed orthogonal frame, i.e. forward-transversal-down.

In the corner steering motion model, the robot turning can be regarded as moving around the virtual point O, and the virtual center wheel's movement direction is always parallel to the carrier's (as shown in figure 3(a)). This model is equivalent to the Ackerman motion model. We can easily obtain the longitudinal velocity by measuring the speed of two middle wheels with an odometer. Assuming that the turning radius is ρ, turning angular velocity is ω, and wheel track is $2d$, then the speeds of the left and right middle wheels are given by

$$\begin{aligned} v_{\mathrm{l}} &= \omega(\rho - d) \\ v_{\mathrm{r}} &= \omega(\rho + d). \end{aligned} \tag{8}$$

The virtual center wheel's longitudinal velocity is

$$v_{\mathrm{odo}} = \omega\rho = \frac{v_{\mathrm{l}} + v_{\mathrm{r}}}{2}. \tag{9}$$

Equation (9) still holds in the all-wheel steering motion model.

If wheels do not skid or jump, the velocity in the plane perpendicular to the longitudinal direction is almost zero according to the NHC. Therefore, the three-dimensional velocity at the virtual center wheel in the w-frame can be expressed as

$$\boldsymbol{v}^{w}_{\mathrm{odo}} = [v_{\mathrm{odo}}\ \ 0\ \ 0]^{T}. \tag{10}$$

Taking the odometer scale factor (s_{odo}) and the velocity measurement noise ($\boldsymbol{e}_v$) into consideration, the w-frame velocity at the virtual center wheel measured with the odometer can be expressed as

$$\tilde{\boldsymbol{v}}^{w}_{\mathrm{odo}} = (1 + s_{\mathrm{odo}})\boldsymbol{v}^{w}_{\mathrm{odo}} + \boldsymbol{e}_v. \tag{11}$$

The v-frame is not parallel to the w-frame in the all-wheel steering motion model, as shown in figure 3(b). Therefore, it is necessary to introduce the wheel angle θ to describe this model. The direction cosine matrix from the v-frame to the w-frame can be written as

$$\begin{aligned} \mathbf{C}^{w}_{v} &= \begin{bmatrix} \cos\theta & \sin\theta & 0 \\ -\sin\theta & \cos\theta & 0 \\ 0 & 0 & 1 \end{bmatrix} \\ \theta &= (\theta_l + \theta_r)/2. \end{aligned} \tag{12}$$

Here, θ is equal to 0 in the corner steering motion model, and thus $\mathbf{C}^{w}_{v}$ degenerates to the identity matrix.

After projecting the velocity derived by INS onto the virtual center wheel in the w-frame, we can obtain

$$\begin{aligned} \boldsymbol{v}^{w}_{\mathrm{odo}} = \boldsymbol{v}^{v}_{\mathrm{odo}} &= \mathbf{C}^{w}_{v}\mathbf{C}^{v}_{b}(\mathbf{C}^{b}_{n}\boldsymbol{v}^{n}_{\mathrm{imu}} + (\boldsymbol{\omega}^{b}_{nb}\times)\boldsymbol{l}^{b}_{\mathrm{odo}}) \\ &= \mathbf{C}^{w}_{v}\mathbf{C}^{v}_{b}(\mathbf{C}^{b}_{n}\boldsymbol{v}^{n}_{\mathrm{imu}} - (\boldsymbol{\omega}^{b}_{in}\times)\boldsymbol{l}^{b}_{\mathrm{odo}} - (\boldsymbol{l}^{b}_{\mathrm{odo}}\times)\boldsymbol{\omega}^{b}_{ib}) \end{aligned} \tag{13}$$

where $\mathbf{C}^{v}_{b}$ is the direction cosine matrix of the IMU mounting angle which is given by the method in [22], $\boldsymbol{v}^{n}_{\mathrm{imu}}$ is the velocity of the IMU, $\boldsymbol{l}^{b}_{\mathrm{odo}}$ is the lever-arm from the IMU to the virtual center wheel, and $(\boldsymbol{\omega}^{b}_{nb}\times)\boldsymbol{l}^{b}_{\mathrm{odo}}$ is the lever-arm effect.

The perturbation model of equation (13) can be expressed as (ignoring second-order small quantities)

$$\begin{aligned} \hat{\mathbf{C}}^{w}_{v} &= \begin{bmatrix} \cos(\theta+\delta\theta) & \sin(\theta+\delta\theta) & 0 \\ -\sin(\theta+\delta\theta) & \cos(\theta+\delta\theta) & 0 \\ 0 & 0 & 1 \end{bmatrix} \\ &\approx \begin{bmatrix} \cos\theta - \sin\theta\delta\theta & \sin\theta + \cos\theta\delta\theta & 0 \\ -\sin\theta - \cos\theta\delta\theta & \cos\theta - \sin\theta\delta\theta & 0 \\ 0 & 0 & 1 \end{bmatrix} \\ &= \mathbf{C}^{w}_{v}\left(\mathbf{I} + \begin{bmatrix} -\sin\theta & \cos\theta & 0 \\ -\cos\theta & -\sin\theta & 0 \\ 0 & 0 & 0 \end{bmatrix}\delta\theta\right) \end{aligned} \tag{14}$$

$$\begin{aligned} \hat{\boldsymbol{v}}^{w}_{\mathrm{odo}} = \hat{\boldsymbol{v}}^{v}_{\mathrm{odo}} &= \hat{\mathbf{C}}^{w}_{b}\mathbf{C}^{v}_{b}[\hat{C}^{b}_{n}\hat{\boldsymbol{v}}^{n}_{\mathrm{imu}} - (\boldsymbol{\omega}^{b}_{in}\times)\boldsymbol{l}^{b}_{\mathrm{odo}} - (\boldsymbol{l}^{b}_{\mathrm{odo}}\times)\hat{\omega}^{b}_{ib}] \\ &= \hat{C}^{w}_{v}\mathbf{C}^{v}_{b}[\mathbf{C}^{b}_{n}(I+\phi\times)(\boldsymbol{v}^{n}_{\mathrm{imu}} + \delta\boldsymbol{v}^{n}_{\mathrm{imu}}) - (\boldsymbol{\omega}^{b}_{in}\times)\boldsymbol{l}^{b}_{\mathrm{odo}} \\ &\quad - (\boldsymbol{l}^{b}_{\mathrm{odo}}\times)(\boldsymbol{\omega}^{b}_{ib} + \delta\boldsymbol{\omega}^{b}_{ib})] \\ &\approx \boldsymbol{v}^{w}_{\mathrm{odo}} + \hat{C}^{w}_{v}\mathbf{C}^{v}_{b}[\mathbf{C}^{b}_{n}\delta\boldsymbol{v}^{n}_{\mathrm{imu}} - \mathbf{C}^{b}_{n}(\boldsymbol{v}^{n}_{\mathrm{imu}}\times)\phi - (\boldsymbol{l}^{b}_{\mathrm{odo}}\times)\delta\boldsymbol{\omega}^{b}_{ib}]. \end{aligned} \tag{15}$$

Combining equations (14) and (15), the w-frame velocity at the virtual center wheel derived by INS can be written as

$$\begin{aligned}\hat{\boldsymbol{v}}^w_{\mathrm{odo}} &= \boldsymbol{v}^w_{\mathrm{odo}} + H_\theta \delta\theta + \mathbf{C}^w_v \mathbf{C}^v_b (\mathbf{C}^b_n \delta \boldsymbol{v}^n_{\mathrm{imu}} \\ &\quad - \mathbf{C}^b_n (\boldsymbol{v}^n_{\mathrm{imu}} \times)\phi - (\boldsymbol{l}^b_{\mathrm{odo}} \times)\delta\boldsymbol{\omega}^b_{ib}) \\ H_\theta &= \begin{bmatrix} -\sin\theta & \cos\theta & 0 \\ -\cos\theta & -\sin\theta & 0 \\ 0 & 0 & 0 \end{bmatrix} \boldsymbol{v}^v_{\mathrm{odo}}. \end{aligned} \tag{16}$$

Combining equations (11) and (16), the w-frame velocity error measurement equation at the virtual center wheel can be expressed as

$$\begin{aligned} z^w_{\mathrm{odo}} &= \hat{\boldsymbol{v}}^w_{\mathrm{odo}} - \tilde{\boldsymbol{v}}^w_{\mathrm{odo}} \\ &= \mathbf{C}^w_v \mathbf{C}^v_b \mathbf{C}^b_n \delta \boldsymbol{v}^n_{\mathrm{imu}} - \mathbf{C}^w_v \mathbf{C}^v_b \mathbf{C}^b_n (\boldsymbol{v}^n_{\mathrm{imu}} \times)\phi \\ &\quad - \mathbf{C}^w_v \mathbf{C}^v_b (\boldsymbol{l}^b_{\mathrm{odo}} \times)\delta\boldsymbol{\omega}^b_{ib} - \boldsymbol{v}^w_{\mathrm{odo}} s_{\mathrm{odo}} + H_\theta \delta\theta - \boldsymbol{e}_v. \end{aligned} \tag{17}$$

In addition, the observation equation can be written as

$$\begin{aligned} z^w_{\mathrm{odo}} &= H_{\mathrm{odo}} \boldsymbol{x} - \boldsymbol{e}_v \\ H_{\mathrm{odo}} &= [0_{3\times3} \;\; \mathbf{C}^w_v \mathbf{C}^v_b \mathbf{C}^b_n \;\; -\mathbf{C}^w_v \mathbf{C}^v_b \mathbf{C}^b_n (\boldsymbol{v}^n_{\mathrm{imu}} \times) \;\; 0_{3\times3} \\ &\quad - \mathbf{C}^w_v \mathbf{C}^v_b (\boldsymbol{l}^b_{\mathrm{odo}} \times) \mathrm{diag}(\boldsymbol{\omega}^b_{ib}) \;\; 0_{3\times3} \;\; \boldsymbol{v}^w_{\mathrm{odo}} \;\; H_\theta] \end{aligned} \tag{18}$$

where H_{odo} is the observation matrix.

For the corner steering motion model, θ in $\mathbf{H}_\theta$ is equal to 0, and $\delta\theta$ is not considered; therefore, equation (17) degenerates into the equation in the conventional vehicular constraint algorithm. Consequently, the GIOW algorithm is compatible with the conventional vehicular constraint algorithm. The conventional vehicular constraint algorithm is just a special case of our proposed GIOW algorithm.

Moreover, the IMU mounting angle ($\mathbf{C}^v_b$) contains error, which is ignored in the conventional vehicular constraint algorithm. The wheel angle error ($\hat{C}^w_v$) estimated in the EKF absorbs part of the error of $\mathbf{C}^v_b$ in the GIOW algorithm.

In addition, in the all-wheel steering motion model, the odometer speed cannot be employed without the wheel angle. However, the wheel angle can be employed independently, and only the NHC is used in this case. The observation equation degenerates to

$$z^w_{\mathrm{odo}} = \begin{bmatrix} v^w_{\mathrm{odo},y} \\ v^w_{\mathrm{odo},z} \end{bmatrix} - \begin{bmatrix} 0 \\ 0 \end{bmatrix} = \begin{bmatrix} H_{\mathrm{odo},y} \\ H_{\mathrm{odo},z} \end{bmatrix} \boldsymbol{x} - \boldsymbol{e}_v. \tag{19}$$

3. Experimental results and discussion

The wheeled robot platform with a six-wheel chassis is shown in figure 4. The odometer speed and the wheel angle of the two middle wheels are derived from the chassis. The odometer resolution is 800 pulses per resolution and the wheel diameter is 15 cm. More information of the robot chassis can be found at www.dalurobot.com/page15.html. In addition, the robot carries two GNSS antennas, a MEMS IMU ADIS16465, and a navigation-grade INS POS620. The front GNSS antenna receives the GNSS signal to provide positioning result for two IMUs. Centimeter-level real-time kinematic (RTK) positioning results are utilized for integrated navigation. The main technical parameters of the two IMUs are listed in table 1. The introduction of reference system and test system are as below.

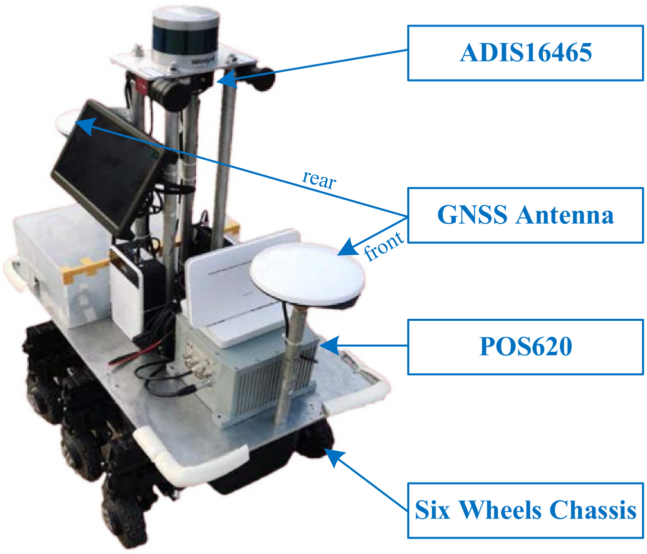

Figure 4. Wheeled robot platform.

Table 1. Technical parameters of the IMUs used in the experiments.

IMU	ADIS16465	POS620
Gyro bias stability (° h^{-1})	2	0.02
Angle random walk (° $(\sqrt{h})^{-1}$)	0.15	0.003
Accelerometer bias stability (mGal)	0.36	0.01
Velocity random walk (m s^{-1} $(\sqrt{h})^{-1}$)	0.012	0.03

The reference system contains the RTK results and the POS620 data. The RTK results and the POS620 data were fused in a commercial integrated navigation software, and the results after reverse smoothing were taken as the ground truth.

The test system contains the RTK results, the ADIS16465 data, the odometer speed and the wheel angle. The RTK results and the ADIS16465 data are collected in a data acquisition module, which is the product of our previous work and takes STM32F767 (ST Microelectronics, 2017) as the control processing core. Time synchronization of all data in the test system is implemented in it. The initial navigation state of the test system needs to be given before data fusion. After the RTK results were available, the test system was stationary for initial alignment. The initial position was provided by the RTK results. We could obtain the initial roll angle and pitch angle through the angular velocity of the earth's rotation and gravity [23]. The initial yaw angle was provided by dual-antenna [24]. To evaluate the performance of the GIOW algorithm, GNSS simulation outages were used in the test system. After the initial alignment of the test system, the RTK results were artificially interrupted for 30 s every 120 s. The test system fused

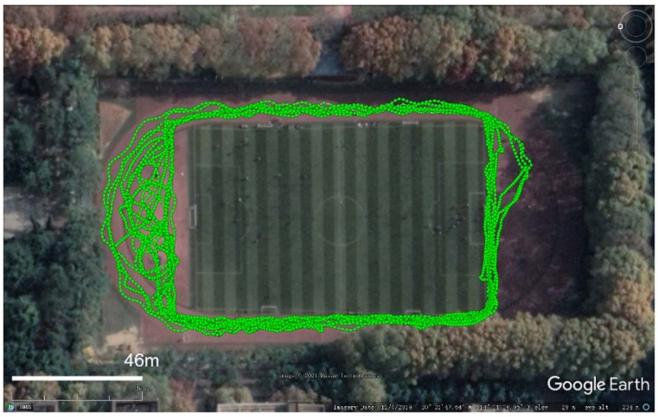

Figure 5. Test trajectory. Map data ©2021 Google.

Table 2. Processing modes in experiment 1 (corner steering only).

Mode	Odometer speed	Odometer scale factor	Wheel angle	Wheel angle error
#1	N	N	N	N
#2	Y	N	N	N
#3	Y	Y	N	N
#4	Y	Y	Y	Y

Mode #1: There is no auxiliary information. This mode is just the GNSS/INS solution, which is in contrast to evaluating the performance of the GIOW algorithm.
Mode #2: On the basis of Mode #1, the odometer speed combined with the NHC are added to constrain the drifting error of the INS. The observation equation in this mode is equation (18), but s_{odo} and $\delta\theta$ are not considered. This mode is set to show the effect of ignoring the odometer scale factor.
Mode #3: On the basis of Mode #2, the odometer scale factor is estimated and compensated. The observation equation in this mode is equation (18), but $\delta\theta$ is not considered. This mode is just the conventional vehicular constraint solution.
Mode #4: On the basis of Mode #3, the wheel angle is considered, and the wheel angle error is estimated and compensated. This mode is the GIOW solution, where the observation equation is equation (18).

the RTK results with outages, the ADIS16465 data, the odometer speed, and the wheel angle to provide continuous and accurate positioning result.

Figure 5 shows the test trajectory, which is in a fully open sky condition. We performed two experiments on the rubber track of a playground. The track could be regarded as a horizontal plain. Experiment 1 was from 438 080 s to 440 180 s (GPS seconds of week), during which the robot's motion was corner steering. Experiment 2 was from 440 180 s to 442 050 s, during which the robot's motion was a mix of corner steering and all-wheel steering.

3.1. Results of experiment 1 (corner steering only)

The corner steering motion model is employed in experiment 1. Four modes are listed in table 2.

The results of the four modes are compared with the truth to obtain the position error, which is shown in figure 6. The RMS of the position error during outages is counted and recorded in table 3.

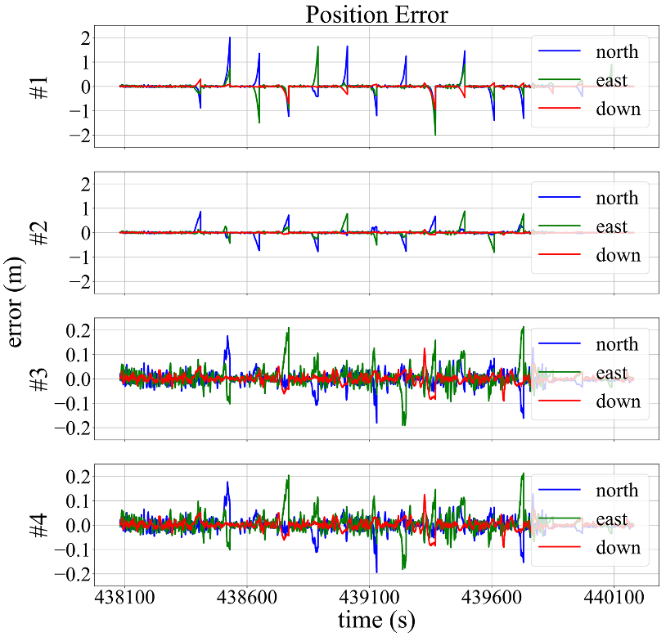

Figure 6. Position error in experiment 1.

Table 3. RMS of position error during outages.

Mode	Horizontal position error (m)	Height error (m)
#1	1.52	0.36
#2	0.67	0.03
#3	0.15	0.03
#4	0.15	0.03

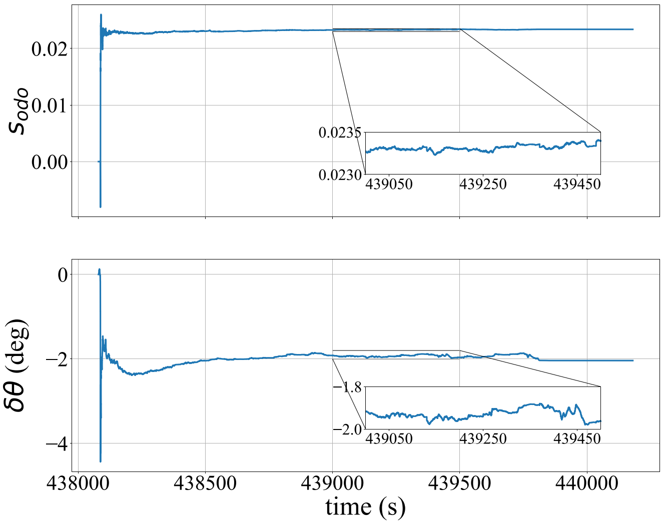

Figure 7. Estimation of s_{odo} and $\delta\theta$.

From table 3, it can be found that the horizontal position error in Mode #2 is reduced by 56% compared to that of Mode #1, and the error in Mode #3 is reduced by 78% compared to that of Mode #2. However, compared to Mode #3, the position error is not obviously changed in Mode #4. This is because the wheel angle is 0° in the corner steering motion model, which

Table 4. Processing modes in experiment 2 (mixed steering).

Mode	Odometer speed	Odometer scale factor	Wheel angle	Wheel angle error
#1	N	N	N	N
#2	N	N	Y	N
#3	N	N	Y	Y
#4	Y	Y	Y	Y

Mode #1: There is no auxiliary information (the GNSS/INS solution).
Mode #2: On the basis of Mode #1, the wheel angle is considered to use the NHC in the w-frame. The observation equation in this mode is equation (19), but $\delta\theta$ is not considered. This mode is set to show the effect of missing the wheel angle error.
Mode #3: On the basis of Mode #2, the wheel angle error is estimated and compensated. The observation equation in this mode is equation (19).
Mode #4: On the basis of Mode #3, the odometer speed is considered, and the odometer scale factor is estimated and compensated (the GIOW solution). The observation equation in this mode is equation (18).

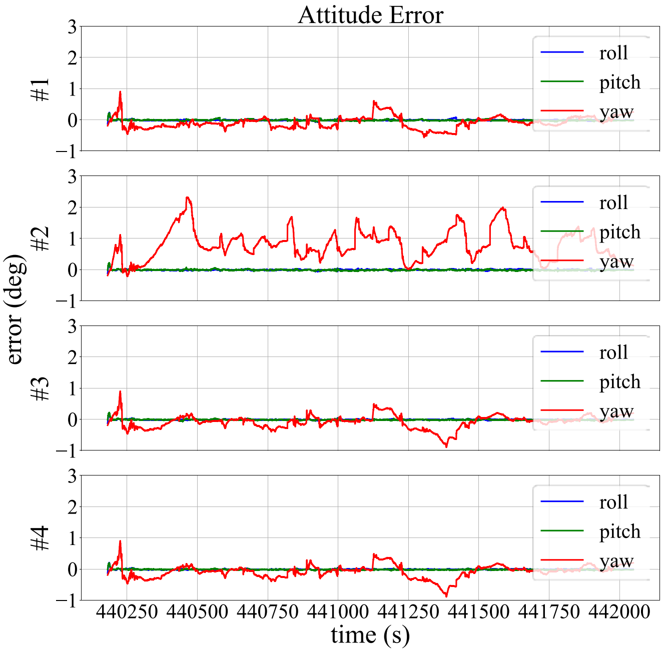

Figure 8. Attitude error in experiment 2.

has little effect in the GIOW algorithm. The experimental results show that the GIOW algorithm has the same performance as the conventional vehicular constraint algorithm in the corner steering motion model. Overall, the horizontal position accuracy of the GIOW algorithm is improved by approximately 90% compared to that of the GNSS/INS solution.

In addition, s_{odo} and $\delta\theta$ are estimated online in Mode #4, and their estimation are shown in figure 7. After convergence, the odometer scale factor is nearly 0.023, and the wheel angle error is nearly $-2.0°$. These error cannot be ignored. The results of Mode #2 show the effect of the odometer scale factor, which decreases the horizontal position error by 78% compared to Mode #3. The effect of the wheel angle error is shown in experiment 2.

Table 5. RMS of attitude error during outages.

Mode	Roll error (°)	Pitch error (°)	Yaw error (°)
#1	0.03	0.04	0.23
#2	0.03	0.02	**0.89**
#3	0.02	0.02	0.23
#4	0.02	0.02	0.22

Note: The yaw angle error of Mode #2 is largest in all four modes.

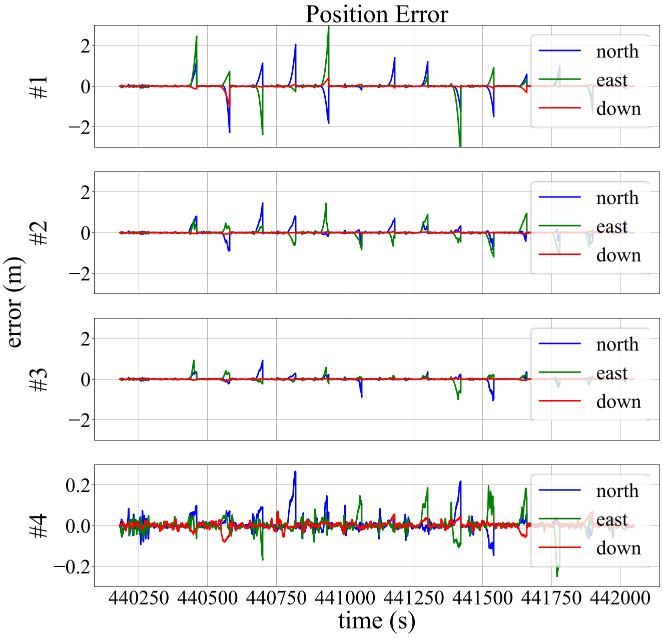

Figure 9. Position error in experiment 2.

3.2. Results of experiment 2 (mixed steering)

The mixed motion of corner steering and all-wheel steering is employed in experiment 2. Since experiment 1 evaluated the effect of the odometer speed and the odometer scale factor, we did not repeat them in experiment 2 and focused on the wheel angle and the wheel angle error. Four modes are listed in table 4.

The attitude error of the four modes is shown in figure 8, and the RMS of this error during outages is recorded in table 5. We find that the yaw angle error of Mode #2 is notably worse than that of the other cases. This is due to the lack of estimation of wheel angle error, which leads to deterioration of the yaw angle accuracy of the navigation system if not compensated. The error is compensated in Modes #3 and #4, and therefore the yaw angle accuracy is at the same level as that of Mode #1.

The position error in experiment 2 is shown in figure 9, and the RMS of this error during outages is recorded in table 6. The horizontal position error is reduced gradually, and the height error is also reduced significantly. Overall, the horizontal position accuracy of the GIOW algorithm is improved by approximately 92% compared to that of the GNSS/INS solution, which has almost the same performance with experiment 1. The experimental results show that the GIOW algorithm can be applicable to the all-wheel steering motion model and

Table 6. RMS of position error during outages.

Mode	Horizontal position error (m)	Height error (m)
#1	2.11	0.31
#2	1.04	0.03
#3	0.66	0.03
#4	0.17	0.03

the corner steering motion model, and the accuracy of the algorithm was maintained.

The estimation of s_{odo} and $\delta\theta$ in Mode #4 is almost equivalent to that in experiment 1.

4. Conclusion

To solve the issue that the conventional vehicular constraint algorithm cannot be applied to robots with the all-wheel steering motion model, we have proposed a GIOW algorithm, which can be applied to the all-wheel steering motion model and the corner steering motion model. The odometer speed and the wheel angle are employed to construct a w-frame velocity observation to constrain the rapid drifting error of INS when the GNSS signal is denied. The source code and a demo for the GIOW algorithm are available at https://github.com/i2Nav-WHU/GIOW-release.

The experimental results showed that the GIOW algorithm has good adaptability in the two motion models. In the corner steering motion model, the same performance as the conventional vehicular constraint algorithm was observed. In the all-wheel steering motion model, to which the conventional constraint algorithm cannot be applied, the accuracy of the GIOW algorithm was maintained. Moreover, the deterioration of the yaw angle accuracy due to the wheel angle error was overcome. An additional benefit of the GIOW algorithm was that the wheel angle error estimated in the EKF could absorb part of the IMU mounting angle error.

In fact, the GIOW algorithm which employs the robot kinematic constraint can be regarded as a general model that covers most of the wheeled carriers with no skidding. The conventional vehicular constraint algorithm is simply a special case of the GIOW algorithm. In future work, we plan to verify and improve the GIOW algorithm on more wheeled robots and engineering vehicles.

Acknowledgments

The authors thank Liqiang Wang for helping us complete the experiments in the paper. The authors also thank Qianxun Spatial Intelligence Inc for their support. This work was also supported in part by the National Key Research and Development Program of China (Grant No. 2020YFB0505803) and the National Natural Science Foundation of China (Grant No. 41974024).

ORCID iDs

Zaixing Zhang https://orcid.org/0000-0001-5426-3613
Hailiang Tang https://orcid.org/0000-0002-5224-036X
Tisheng Zhang https://orcid.org/0000-0001-7602-0428

References

[1] Lv W 2020 Information fusion algorithm of GNSS/INS integrated navigation system. *J Phys. Conf. Ser.* **1544** 012005

[2] Mostafa M Z, Khater H A, Rizk M R and Bahasan A M 2019 A novel GPS/RAVO/MEMS-INS smartphone-sensor-integrated method to enhance USV navigation systems during GPS outages *Meas. Sci. Technol.* **30** 095103

[3] Chen C and Chang G 2019 Low-cost GNSS/INS integration for enhanced land vehicle performance *Meas. Sci. Technol.* **31** 035009

[4] Shi B, Wang M, Wang Y, Bai Y, Lin K and Yang F 2021 Effect analysis of GNSS/INS processing strategy for sufficient utilization of urban environment observations *Sensors* **21** 620

[5] Semeniuk L and Noureldin A 2006 Bridging GPS outages using neural network estimates of INS position and velocity errors *Meas. Sci. Technol.* **17** 2783

[6] Vagle N, Broumandan A and Lachapelle G 2018 Multiantenna GNSS and inertial sensors/odometer coupling for robust vehicular navigation *IEEE Internet Things J.* **5** 4816–28

[7] Niu X, Nassar S and El-sheimy N 2007 An accurate land-vehicle MEMS IMU/GPS navigation system using 3D auxiliary velocity updates *Navigation* **54** 177–88

[8] Moussa M, Moussa A, Elhabiby M and El-Sheimy N 2020 Wheel-based aiding of low-cost IMU for land vehicle navigation in GNSS challenging environment *2020 IEEE 92nd Vehicular Technology Conf. (Vtc2020-fall)*: IEEE) pp 1–6

[9] Broumandan A and Lachapelle G 2018 Spoofing detection using GNSS/INS/Odometer coupling for vehicular navigation *Sensors* **18** 1305

[10] Howard T M and Kelly A 2016 Optimal rough terrain trajectory generation for wheeled mobile robots *Int J Rob Res* **26** 141–66

[11] Jingang Y, Hongpeng W, Junjie Z, Dezhen S, Jayasuriya S and Jingtai L 2009 Kinematic modeling and analysis of skid-steered mobile robots with applications to low-cost inertial-measurement-unit-based motion estimation *IEEE Trans. Robot.* **25** 1087–97

[12] Alves S F, Rosario J M, Ferasoli Filho H, Rincon L, Yamasaki R and Barrera A 2011 Conceptual bases of robot navigation modeling control and applications *Adv. Robot. Navig.* p 26

[13] Gao J, Petovello M and Cannon M E 2008 Integration of steering angle sensor with global positioning system and micro-electro-mechanical systems inertial measurement unit for vehicular positioning *J. Intell. Transp. Syst.* **12** 159–67

[14] Gao J 2007 *Development of a precise GPS/INS/on-board vehicle sensors integrated vehicular positioning system* University of Calgary

[15] Dixon R, Bobye M, Kruger B and Jacox J 2020 GNSS/INS sensor fusion with on-board vehicle sensors *Proc. of the 33rd Int. Technical Meeting of the Satellite Division of the Institute of Navigation (ION GNSS+ 2020)* pp 424–46

[16] Lv W 2020 Kalman filtering algorithm for integrated navigation system in unmanned aerial vehicle *J. Phys. Conf. Ser.* **1575** 012034

[17] Wen W, Pfeifer T, Bai X and Hsu L-T 2020 Comparison of extended Kalman filter and factor graph optimization for GNSS/INS integrated navigation system (arXiv:2004.10572)

[18] Shin E-H 2005 Estimation techniques for low-cost inertial navigation *UCGE Report* 20219

[19] Zhang Q, Niu X, Chen Q, Zhang H and Shi C 2013 Using Allan variance to evaluate the relative accuracy on different time scales of GNSS/INS systems *Meas. Sci. Technol.* **24** 085006

[20] Zhang Q, Niu X and Shi C 2020 Impact assessment of various IMU error sources on the relative accuracy of the GNSS/INS systems *IEEE Sens. J.* **20** 5026–38

[21] Li L, Sun H, Yang S, Ding X, Wang J, Jiang J, Pu X, Ren C, Hu N and Guo Y 2018 Online calibration and compensation of total odometer error in an integrated system *Measurement* **123** 69–79

[22] Chen Q, Zhang Q and Niu X 2020 Estimate the pitch and heading mounting angles of the IMU for land vehicular GNSS/INS integrated system *IEEE Trans. Intell. Transp. Syst.* 1–13

[23] Chuanbin Z, Weifeng T and Zhihua J 2004 A novel method improving the alignment accuracy of a strapdown inertial navigation system on a stationary base *Meas. Sci. Technol.* **15** 765

[24] Schnaufer B, McGraw G, Phan H and Joseph A 2016 GNSS-based dual-antenna heading augmentation for attitude and heading reference systems *Proc. 29th Int. Technical Meeting of the Satellite Division of the Institute of Navigation (ION GNSS+ 2016)* pp 3669–91